Waste valorization: Transforming the fishbone biowaste into biochar as an efficient persulfate catalyst for degradation of organic pollutant

Xiaoya Ren [a,b], Jingjing Wang [a,b], Jiangfang Yu [a,b], Biao Song [a,b] , Haopeng Feng [a,b], Maocai Shen [a,b], Hao Zhang [a,b], Jiajing Zou [a,b], Guangming Zeng [a,b] *, Lin Tang [a,b] *, Jiajia Wang [a,b] *

[a] College of Environmental Science and Engineering, Hunan University, Changsha, 410082, China;

[b] Key Laboratory of Environmental Biology and Pollution Control, Hunan University, Ministry of Education, Changsha 410082, China;

* Corresponding Authors

E-mail: zgming@hnu.edu.cn (Guangming Zeng), tanglin@hnu.edu.cn (Lin Tang), wangjiajia07@hnu.edu.cn (Jiajia Wang)

Abstract

Fishbone is a major by-product of fishing processing and how to deal with the increasingly generated fishbone has been a big challenge. In an effort to convert the low-value waste into valuable material, this research explores the valorization of fishbone biowaste, which can be transformed into biochar as a persulfate activator for phenol removal. The fishbone derived biochar (FBBC) was prepared by one-step pyrolysis without additional template. The catalytic efficiency of FBBC increases with pyrolysis temperature, with FBBC-800 (pyrolyzed at 800 °C) exhibiting the best performance of 100% phenol (20 mg/L) removal within 60 min at the catalyst dosage of 0.1 g/L, which is comparable to other recently reported carbon-based catalysts but with the advantage of easy preparation, low cost and wastes valorization. The high efficacy of FBBC-800 is related to its large surface area (758.44 m^2/g), carbonyl group and defective structure. In the FBBC-800/ peroxydisulfate /phenol system, both radical and non-radical pathways are involved, among which hydroxyl radical is more important in radical pathway while singlet oxygen dominates in non-radical pathway. Electron transfer plays a key role in this process through electron capture experiment and electrochemical characterization. This study proposes a new strategy for the valorization of fishbone, and provides the guidance for the structure design of carbon-based catalyst for persulfate activation.

Keywords: Waste valorization, Calcium rich biowaste, Fishbone biochar, Persulfate activation

1. Introduction

The global fish production has been increasing over recent years, from 20 million tons in 1950 up to 179 million tons in 2018, and is projected to reach 204 million tons in 2030 (FAO, 2020). This is accompanied with a large amount of fishery wastes, with a estimation of over 20 million tons per year (Nawaz et al., 2020). Fishbone is the main by-product from fish processing, accounting for 8%-10% of total fish biomass (Yin et al., 2015). In many cases, fishbone is discarded directly or used for low value fish meal production, which is a waste of resources (Marti-Quijal et al., 2020). Some efforts have been made on extraction of substance (e.g. hydroxyapatite, gelatin and bioactive calcium, etc) from fishbone for human consumption (Akagündüz et al., 2014; Boutinguiza et al., 2012; Zhang et al., 2016). However, it is still challenging for large scale application and the food safety issues are seriously concerned (Nawaz et al., 2020). Pyrolysis is a good way to achieve the valorization of fishbone as it is convenient and simple, and the resultant biochar product can be developed for various applications (Kim et al., 2020). Fishbone is a natural composite of organic (21%-57%) and inorganic substance (31%-73%) (Toppe et al., 2007). The organic portions such as collagen, proteins and fats serve as carbon precursors, and nanohydroxyapatite, the major inorganic mineral present in bone act as self-template. Such unique characteristics make it a perfect material for biochar preparation. Although previous studies have explored the application of fishbone in the catalyst reaction, either it is used as a catalyst support (Chakraborty and RoyChowdhury, 2013) or some chemical agents (e.g.

KOH and $FeCl_3$) are used during the catalyst preparation process (Wang et al. 2015; Niu et al. 2019a). The inherent catalytic ability was ignored and the complicated production process would also increase the costs. This study makes full use of the self-template in fishbone to prepare porous carbon catalyst, and the preparation process is simple and environmental friendly. In addition, currently, fishbone derived biochar (FBBC) has been applied in electro-catalysis, supercapacitor and pollutant adsorption (Medell ń-Castillo et al., 2020; Niu et al., 2019a; Wang et al., 2015), which proves the possible adsorption and catalytic ability. However, utilizing FBBC as a catalyst for pollutant degradation has rarely been reported. As a good electron donor and electron carrier, FBBC might be exploited in the persulfate-induced advanced oxidation processes (PS-AOPs).

The PS-AOPs is a kind of water treatment technology and has attracted more and more interest in recent years due to its easy operation and high mineralization efficiency. Peroxydisulfate (PDS) is a stable oxidant with low oxidative potential for pollutant degradation (Wacławek et al., 2017). However, the peroxide O–O bond in PDS can be cleaved with the assistance of catalysts or external energy, along with the generation of highly reactive species including hydroxyl radicals ($^{\cdot}OH$) and sulfate radicals ($SO_4^{\cdot-}$), which enables the effective degradation of refractory organics (Duan et al., 2015). Various methods have been used for PDS activation, such as UV irradiation, thermal, ultrasound, transition metals and carbonaceous materials (Wang and Wang, 2018). Among these methods, biochar exhibits unique benefits of low cost, rich feedstock sources and simple preparation process (Ye et al.,

2019). However, to overcome the problem of unsatisfactory catalytic ability in pristine biochar, heteroatom or metal doping have been applied to improve the reactivity of biochar (Fang et al., 2015; Wang et al., 2019a), but this comes out at the cost of excessive synthesis cost or metal leaching. Consequently, attention has been directed toward the structure and chemical constitution of biomass for biochar production. For example, Chen et al. (2019) employed Fe/N abundant *Enteromorpha* biomass for preparing carbocatalyst and used it for peroxymonosulfate activation. The intrinsic N derived from *Enteromorpha* provide the active site for paracetamol degradation. Similarly, Ma et al. (2018) synthesized N/S co-doped porous carbon from human hair, which exhibited better degradation efficiency of bisphenol A than some metal-based catalysts in PDS system. However, KOH as the activator was used in those studies to form porous structure, which is corrosive to the equipment. Biowaste with abundant elements such as K, Na and Ca is a good choice of biochar raw material, which provide the possibility of in-situ activation during the pyrolysis process.

Inspired by above results, we believe that FBBC would exhibit excellent activity for PDS activation. The porous structure derived from nanohydroxyapatite self-template is favorable for the catalytic reaction (Alhokbany et al., 2019). On the one hand, the well-developed porous structure exposes more active site for catalysis. On the other hand, the intensified adsorption of organic pollutants around the active site facilitate the subsequent catalytic degradation. In addition, electron transfer is an important process in the catalytic reaction (Ren et al., 2019; Yang et al., 2018).

Wang et al. (2015) have studied the electrocatalytic performance of fishbone carbon in the oxygen reduction reaction, and it showed high electron transfer capacity.

Based on the peculiar component of fishbone and the concept of waste valorization, we choose fishbone as a raw material to prepare biochar. The FBBC was applied to activate PDS for degradation of a model pollutant (phenol), where the impact of biochar pyrolysis temperature was studied. The possible catalytic site responsible for the activation reaction was explored. Radical quenching experiments, electron spin resonance and electrochemical characterization were conducted to reveal the activation mechanism. The removal efficiency of phenol in real samples were also investigated. This research proposes a new route for fishbone valorization, with both the advantage of reducing biowaste disposal cost and creating effective catalyst for pollutant removal. It is expected that this study would shed light on the biomass selection and structural regulation of biochar to get excellent catalytic efficiency.

2. Materials and methods

In this section, firstly, the specific information about the chemicals and materials used in this study is provided. Secondly, the preparation process of FBBC catalyst is described. Then the techniques used to characterize the structural properties of FBBC are summarized. At last, the detailed reaction procedure and reaction parameters are presented.

2.1. Chemicals and materials

The abyssal fishbone was obtained from a fish processing factory in Weihai,

China. All the chemicals used in this study were used at analytical grade (details can be seen in Text S1). Ultrapure water (18.25 MΩ/cm) was used throughout the experiment.

2.2. Preparation of biochar

FBBC was prepared as described previously with some modification (Wang et al. 2015). Fishbone was washed with deionized water for several times and dried in the oven for 24 h. Then the dried sample was smashed into powder, screened by 100 mesh sieves and pyrolyzed in a quartz tube furnace at different temperatures (400 ℃, 600 ℃ and 800 ℃) for 2 h under nitrogen environment (nitrogen flow rate of 100 mL/min, heating rate of 5 ℃/min). After cooling to room temperature, the obtained product was washed with 2M HCl for 24 h to remove the calcium compounds. Subsequently, the product was rinsed by ultrapure water until the pH of filtrate present neutrality and dried at 60 ℃ for 24 h. The final sample was designated as FBBC-400, FBBC-600 and FBBC-800, corresponding to the pyrolysis temperature of 400 ℃, 600 ℃ and 800 ℃, respectively. Details about the yield of FBBC can be seen in Text S2.

2.3. Characterization

The structure and morphology of FBBC were observed by scanning electronic microscopy (SEM, Nova NanoSEM230) and high-resolution transmission electron microscopy (HRTEM, Tecnai G2 F20). The pore size distribution and specific surface area were measured by the Quantachrome NovaWin (NOVA 2000e) and the degassing conditions are 300 ℃ for 4 h. The surface functional groups were

investigated by a Fourier-transform infrared spectroscopy (FTIR). Raman spectra were investigated at the excitation wavelength of 532 nm, accompanied with the range from 100 to 4000 nm. X-ray photoelectron spectroscopy (XPS) was conducted on Thermo Escalab 250XI. Zeta potential was obtained from the Zetasizer Nano (Zetasizer Nano ZSP). Electrochemical measurements details including electrochemical impedance spectroscopy (EIS), liner sweep voltammetry (LSV) and chronoamperometric measurements were appended in Text S3.

2.4. Catalytic tests and active species detection

The catalytic oxidation experiment of phenol was conducted in a thermostatic oscillator (170 rpm, 25 ℃). Unless otherwise stated, 3 mg FBBC and 30 mg PDS were added into 30 mL of phenol solution (20 ppm) to initiate the degradation reaction. At specific time intervals, 1 mL of samples was withdrawn, filtered by 0.45 μm membrane and detected for phenol concentration immediately. The adsorption experiment was performed in the same conditions without the addition of PDS. The experimental parameter selection was provided in Text S4. Phenol concentration was analyzed using a high-performance liquid chromatography (acetonitrile/water=30/70, volume ratio) at the wavelength of 270 nm. All the experiments were conducted in triplicate.

Pseudo-first order kinetic model with high values of R^2 was used to mimic the phenol degradation curves in this study. The reaction rate constant k_{obs} was calculated by Eq. (1) and Eq. (2):

$$-dC/dt = k_{obs}C \quad \text{Eq. (1)}$$

$$\ln (C_t/C_0) = -k_{obs}t \quad \text{Eq. (2)}$$

C_t is the concentration of phenol at reaction time t, and C_0 is the initial concentration of phenol.

To identify the roles of reactive radicals in the degradation process, different molar ratios of radical scavengers (methanol (MeOH), tert-butyl-alcohol (TBA) and ethanol (EtOH)) were added into the reaction system for the quenching of $SO_4^{\cdot -}$ and $^{\cdot}OH$. Besides, 10 mM of p-benzoquinone (BQ), NaN_3 and K_2CrO_4 were used to scavenge superoxide radical ($O_2^{\cdot -}$), singlet oxygen ($^1O_2$) and free electrons, respectively. An electron spin resonance spectrometer (ESR; JEOL FA200) with 5,5-dimethyl-1-pyrroline N-oxide (DMPO) and 2,2,6,6-tetramethyl-4-piperidinol (TMP) as capture agent was also used to determine the generated active radicals.

3. Result and Discussion

3.1. Morphological characterization of FBBC

The morphology and structure characterization of FBBC are investigated by SEM and TEM. It is observed from Fig. 1a-b that FBBC-800 exhibits rough, wrinkle-rich surface, accompanied with high specific area of 758.44 m^2/g (Table S1). It is estimated that the high specific area of FBBC-800 is caused by the nanohydroxyapatite self-template, which is inserted into the carbon frame to generate micro-pores during pyrolysis, and then can be mostly removed from the product by diluted acid solution (Medellin-Castillo et al., 2014). As can be seen from Fig 1c, some spiral stripe-like nanosheet are observed in FBBC-800, which could be the stacked graphite layers formed by strong π-π interactions. TEM

mapping shows the existence of C, O and N, among which the N element may be derived from proteins and fats (Fig. 1d-f). The average pore size of FBBC-800 is determined to be 1.17 nm, showing the micro-pore structure (Table S1). The higher specific area and abundant micro-pore structure of FBBC-800 would provide more active site for the catalytic reaction. Besides, the porosity of biochar is largely affected by pyrolysis temperature. As shown in Fig. S1, FBBC-400 presents a relative blocked structure. With the increase of pyrolysis temperature, the structures of solid biochar become condensed and more volatile organic matter (e.g. bio-oil) and gases (e.g. CO_2, CH_4, CO, H_2) are generated (Kambo and Dutta, 2015). The loss of those volatile compounds contributes to the developed pores in biochar. Moreover, at higher pyrolysis temperature, the pyrolysis process transitioned from the liquification reactions (generation of bio-oil) to the release of gasses, and further went through some self-activation process (Eq. (3-6)) (Bommier et al., 2015; Niu et al. 2019b). Therefore, higher pyrolysis temperature leads to a significant enhancement of porosity. The specific area of FBBC is in the order of FBBC-400 (0.48 m^2/g) < FBBC-600 (343.41 m^2/g) < FBBC-800 (758.44 m^2/g) (Table S1), which is in line with the results of SEM and TEM images (Fig. S1).

$$C + H_2O \rightarrow CO + H_2 \quad \text{Eq. (3)}$$

$$C + CO_2 \rightarrow 2CO \quad \text{Eq. (4)}$$

$$C + 2H_2 \rightarrow CH_4 \quad \text{Eq. (5)}$$

$$2Ca_6(PO_4)_3(CO_3)(OH) \rightarrow 2Ca_{6-\gamma}(PO_4)_3(CO_3)_{1-\gamma}O_{\chi/2}(OH)_{1-\chi} + 2\gamma CaO + \chi H_2O + 2\gamma CO_2 \quad \text{Eq. (6)}$$

3.2. Catalytic degradation performance

As the structure of biochar is largely affected by the pyrolysis temperature, three kinds of FBBC prepared at 400 ℃, 600 ℃ and 800 ℃ are studied and their catalytic performance is evaluated by the degradation of phenol (a model pollutant). As shown in Fig. 2a, adsorption contributes a little to the removal of phenol. Among all the biochar samples, FBBC-800 presents the highest adsorption capacity, with 10.7% of phenol removal within 60 min, followed by the order of FBBC-600 (5.5%) and FBBC-400 (1.2%). This result proves the low potential of FBBC as adsorbents for direct application (Naushad et al., 2019a). The higher adsorption capacity of FBBC-800 was probably ascribed to the larger specific surface area (758.44 m^2/g) and strong π-π interaction (Senthil Kumar et al., 2011). Chemical oxidation of phenol by PDS was displayed in Fig. 2b. Notably, PDS alone could hardly degrade phenol. However, in the presence of both FBBC (0.1 g/L) and PDS (1 g/L), the removal efficiency of phenol has significantly improved, with the order of FBBC-800> FBBC-600 > FBBC-400. FBBC-800 exhibits the best catalytic performance of 100% phenol removal in 60 min. Therefore, FBBC-800 was selected as the representative catalyst for the subsequent research. The degradation efficiency was comparable or even better than other metal-free catalyst (Table S2). More importantly, this material was much easier to prepare and cost effective.

As the concentration of PDS rising from 0.5 to 2 g/L, the rate constant k_{obs} increased from 0.06119 to 0.10886 min^{-1}, due to more reactive radicals produced with higher PDS amount (Fig. 2c). However, further increasing the PDS dosage to 3

g/L resulted in a minor decrease in k_{obs}, which could be explained by the self-quenching of excessive radicals (Tang et al., 2018). The effect of FBBC dosage was studied in Fig. 2d. With the increase of FBBC dosage from 0.33 to 1.33 g/L, an enhanced removal of phenol was achieved, along with the rate constant k_{obs} from 0.01082 to 0.11827 min^{-1}. Higher dosage of FBBC provides more catalytic site for both adsorption and oxidation, and increases the effective collision between catalyst and pollutant, contributing to better removal capacity for phenol (Wang et al. 2019a). Taken together the reaction rates and reaction cost, 1 g/L PDS and 0.1g/L FBBC was selected for the subsequent experiment.

The initial pH of the solution is another factor that influences the catalytic capacity of FBBC (Qin et al. 2019). As is shown in Fig. 2e, no obvious change in phenol degradation was observed with the pH ranging from 3 to 9, indicating the wide applicability of FBBC-800/PDS system for practical water treatment. Besides, a slight enhancement in degradation can be seen as the increase of initial pH, with the maxima k_{obs} of 0.10603 min^{-1} at the pH of 9. Duan et al. (2016a) reported that OH^- was easier to donate an electron to PDS than H_2O molecules to produce hydroxyl radicals, which might be the reason for the facilitated PDS activation at pH=9. However, at strong alkaline condition (pH=11), the removal efficiency of phenol sharply declined (59%), along with the k_{obs} down to 0.01352 min^{-1}. The electrostatic repulsion between phenol and FBBC-800 was responsible for the decrease in phenol removal (Dhiman et al., 2017; Kumar et al., 2018). The surface of FBBC-800 was negatively charged at pH >3 (Fig. S2). In addition, the pK_a of

phenol was 9.95, indicating that phenol existed in the form of $C_6H_5O^-$ at pH > 9.95 (Sun et al., 2020). Therefore, the interaction between FBBC-800 and phenol was not favored.

The influence of initial phenol concentration was also investigated and presented in Fig. 2f. It was clear that 100% of phenol removal was achieved at phenol concentration of 10 mg/L, and 70.8% removal was still obtained at higher phenol concentration of 40 mg/L, which manifested the good performance of FBBC-800/PDS system under different concentrations. However, the rate constant k_{obs} decreased from 0.1865 to 0.01864 min^{-1} with the increasing of initial phenol concentration from 10 to 40 mg/L. This could be that high pollutant concentration resulted in the over-occupied active sites and decreased the catalytic activity of FBBC-800 for PDS activation (Alshehri et al., 2014).

3.3. Identification of reactive species

Until now, both radical routes and non-radical routes have been proved in catalyst/PDS system. To verify the involvement of radical in this reaction, radical quenching experiments were carried out (Song et al., 2019). Firstly, MeOH (k_{SO4}·- and k_{OH} are 1.1×10^7 M^{-1} s^{-1} and 9.7×10^8 M^{-1} s^{-1}, respectively) and TBA (k_{SO4}·- and k_{OH} are 4×10^5 M^{-1} s^{-1} and 6×10^8 M^{-1} s^{-1}, respectively) were used as radicals scavengers for quenching the ·OH and SO_4·- (Buxton et al., 1988; Neta et al., 1988). As presented in Fig. 3a-b, both MeOH and TBA have suppressed phenol degradation. Addition of MeOH resulted in an insignificant decrease of phenol degradation (83.28% removal), even with high dose [MeOH /PDS=1000].

Surprisingly, TBA at low amount [TBA /PDS=100] brought minor inhibition effect (93.13% removal) on phenol degradation, but exhibited significant quenching effect (34.94% removal) at high amount [TBA /PDS=1000]. Generally, MeOH was supposed to have comparable or even better inhibition effect in PDS than TBA, as MeOH was reactive with both $SO_4^{\cdot-}$ and ·OH but TBA had higher reactive rate with ·OH. The contradictory phenomena in this study may be related to the following two aspects: 1) Although one molecule MeOH could react with one molecule $SO_4^{\cdot-}$, the resultant CH_2OH ·could again react with PDS to produce $SO_4^{\cdot-}$ and directly involve in phenol degradation (Yu et al., 2019). Consequently, the inhibition effect of MeOH is alleviated, which is consistent with the previous study (Bao et al., 2018). 2) TBA had stronger affinity with FBBC-800 due to the hydrophobic interaction, and impeded the access of PDS and phenol to FBBC-800. In addition, ethanol (EtOH) was also reported to exhibit high rate for both $SO_4^{\cdot-}$ and ·OH ($k_{SO4\cdot-}$ and k_{OH} are 10^7 M^{-1} s^{-1} and 10^9 M^{-1} s^{-1}, respectively) (Sun et al. 2020). Fig. 3c showed that only about 68.1% phenol was removed with high concentration of EtOH. Totally, the radical quenching experiment indicated that both $SO_4^{\cdot-}$ and ·OH participated in the reaction. However, the remained high removal of phenol even when radicals were captured implied the possible existence of other reactive species. Then, BQ was used to confirm the involvement of $O_2^{\cdot-}$ ($k_{O2\cdot-}$= 1×10^9 M^{-1} s^{-1}) (Naushad et al., 2019b； Rao and Hayon, 1975). As presented in Fig. 3d, BQ moderately suppressed phenol removal, verifying the involvement of $O_2^{\cdot-}$ in phenol degradation. $^1O_2$, as a reactive oxygen species derived from

non-radical pathway, was confirmed by quencher NaN_3 (Oh et al., 2018; Zhu et al., 2018). An evident inhibiting effect was observed after addition of NaN_3, with only about 42% phenol removal (Fig. 3d), indicating that $^1O_2$ played an important role in this reaction.

To further identify the existence of radicals in FBBC-800/PDS system, ESR spectroscopy was conducted with DMPO and TMP as spin trapping agents (Fig. 4). When PDS was used alone, no radical signal peak was detected. However, when PDS and FBBC-800 was simultaneously added, the signal peak of DMPO-OH (four lines in 1:2:2:1; $\alpha_N=\alpha_H=14.9$ G) and DMPO-SO_4 (six lines in 1:1:1:1:1:1; $\alpha_N=13.2$ G, $\alpha_{\gamma\text{-}H}=1.48$ G, $\alpha_{\gamma\text{-}H}=0.78$ G, $\alpha_{\beta\text{-}H}=9.6$ G,) were obviously observed and DMPO-OH had higher relative intensity than DMPO-SO_4 (Fig. 4a). This confirmed the existence of $SO_4^{\cdot-}$ and $^{\cdot}OH$, and a higher amount of $^{\cdot}OH$ than $SO_4^{\cdot-}$. Besides, as the reaction proceeded, an increasing trend of the signal intensities was observed, implying the continuous production of radicals. In addition, four characteristic peaks of DMPO-OOH belonging to $O_2^{\cdot-}$ were also found in Fig. 4b. When TEMP was added, triple signal peak with an equal height signal (three lines in 1:1:1, splitting constants of $\alpha_N=16.9$ G) was obviously seen (Fig. 4b). Combining with the radical quenching experiments and ESR analysis, it can be inferred that $SO_4^{\cdot-}$, $^{\cdot}OH$, $O_2^{\cdot-}$ and $^1O_2$ all take part in the reaction, among which $^{\cdot}OH$ and $^1O_2$ play a dominate role.

3.4. The structure changes and surface investigation

The morphological changes of FBBC-800 before and after reaction were

investigated by SEM, which showed no significant difference (Fig. S4). Besides, the porosity is also important for a catalyst. It is well known that porous structure facilitates adsorption of pollutant and contributes to more exposed active sites for the reactions (Wang et al. 2019b). Ho et al. (2019) found that spirulina residue pyrolyzed at 900 ℃ showed 100% sulfamethoxazole removal in PDS system while the desalted spirulina residue pyrolyzed at 900 ℃ displayed only 5.2% sulfamethoxazole removal, due to the extremely lower surface area of the latter than the former. In this study, FBBC-800 without HCl treatment had lower specific area (96.752 m^2/g) than FBBC-800 (758.44 m^2/g) (Table S1), accompanied with about 57.2% phenol removal (Fig. S3a), which indicated the importance of catalyst porosity in PDS system. Consistently, the higher specific area of FBBC-800 (758.44 m^2/g) than FBBC-600 (343.41 m^2/g) and FBBC-400 (0.48 m^2/g) may partially explain its higher catalytic efficiency. To examine the porosity change of FBBC-800 after reaction, N_2 adsorption-desorption isotherms was performed, which was shown in Fig. 5a-b. The isotherm curve as presented in Fig. 5a is a typical type I curve, showing the characteristic of micro-pore, which is consistent with the result of pore size distributions curves. Compared with fresh FBBC-800, the specific surface area and total pore volume of used FBBC-800 reduced by 19.7% and 16.3%, respectively. The decline in specific area after reaction may be ascribed to adsorption of intermediates, and the consequently blocked active site. However, in our study, the specific surface area of used FBBC-800 is not significantly decreased relative to fresh FBBC-800, implying that blocked porosity may not be the main

reason for the deterioration of catalyst (Fig. S3b).

Moreover, the surface change of FBBC-800 after reaction was investigated. Many kinds of oxygen-containing groups have been reported to influence the catalytic activity of carbon-based catalyst, including carboxyl (O=C-OH), carbonyl (C=O) and hydroxyl (C-OH). Duan et al. (2016b) conducted a theoretical calculation and identified the electron-rich ketonic group (C=O) as the primary active site for peroxymonosulfate activation among the oxygen-containing groups. The oxygen atom with lone-pair electrons in ketonic group present high affinity with peroxymonosulfate and promote the electron transfer process. Fig. S5 presented the FTIR of FBBC-800 before and after reaction. The band around 3389 cm^{-1} was attributed to the -OH stretching vibration and 2859-2925 cm^{-1} was derived from aliphatic C-H stretching vibration (Zhao et al. 2016). The distinct peak at 1584 cm^{-1} might belong to the aromatic C=C stretching (Tang et al. 2018). The band for C=O stretching at about 1696 cm^{-1} was also observed (Zhao et al. 2016). In addition, the peak at 1183 cm^{-1} was ascribed to C-OH vibration (Zhang and Wang. 2016). After reaction, the intensity for –OH vibration increased and for C=O vibration decreased, which suggested the possible conversion of the two groups during the catalytic reaction. For further analysis, XPS survey of FBBC-800 was conducted (Fig. 5c). It was apparent to see three distinct peaks at around 285.19 eV, 400.19 eV and 532.19 eV, corresponding to C1s, N1s, and O1s. Clearly, after reaction, the O content in FBBC-800 increased from 9.18% to 13.10%, which revealed that the surface of FBBC-800 was oxidized during PDS activation. This

364 can be explained in two ways (Tang et al., 2018). On the one hand, surface
365 functional groups act as electron transfer intermediate and are oxidized by providing
366 electrons to activate PDS. On the other hand, the production of abundant radicals
367 leads to a highly oxidative environment around FBBC-800, eventually inducing the
368 surface oxidation. The O1s spectra of the fresh FBBC-800 could be fitted into three
369 main peaks at 530.51, 531.31 and 532.84 eV, assigning to O=C-OH, C=O and
370 C-OH, respectively. It was observed that after reaction both the content of O=C-OH
371 and C=O decreased, from 11.5% to 3.6% and 33.5% to 23.4%, respectively,
372 accompanied with the increase of C-OH (from 55% to 73%) (Fig. 6a and c). This
373 indicated the conversion of C=O to C–OH during the catalytic process. In addition,
374 nitrogen doping is an efficient way to improve the reactivity of carbon-based
375 catalyst. The main peak of N1s around 398.36 eV and 400.37 eV was assigned to
376 pyridnic N and pyrrolic N (Fig. 6b). Chen et al. (2019) reported that graphitic N had
377 high adsorption energy with PMS and thus promote PMS activation. Wang et al.
378 (2019a) claimed that edge nitrogen configurations such as pyrrolic N and pyridinic
379 N might be the active site for PDS activation. However, the close ratio of pyridnic
380 N and pyrrolic N before (20%:80%) and after (17.36%:82.64%) reaction indicates
381 that nitrogen element may not act as the catalytic site for PDS activation in this
382 study (Fig. 6b and d). The decline in the relative content of N was likely due to the
383 introduced exogenous oxygen rather than the catalytic loss.

384 The defective edge of carbon materials has also been identified as catalytic
385 sites for PDS oxidation. Raman spectra, a powerful technique for exploring the

crystalline structure of carbon materials, were conducted and the related parameter I_D/I_G (an indicator of disorder degree) was calculated. As shown in Fig. 5d, two important characteristics peaks appeared at FBBC-800 both before and after reaction, where the D peak (1350 cm^{-1}) represented the disorder degree and G peak (1600 cm^{-1}) reflected the graphitization level of carbon materials. Compared to original, the I_D/I_G of FBBC-800 after reaction decreased from 0.972 to 0.945, indicating the decrease of disorder degree. This was probably caused by the break of defective edge, alteration of surface functional group and the adsorption of organic matters on sp^2 hybridized carbon (Tang et al. 2018). Based on above studies, we suppose that the reduced defective sites in FBBC800-used may be responsible for the deterioration of catalytic performance.

3.5 Electron transfer pathway

Based on above analysis, the catalytic mechanism of phenol in FBBC-800/PDS system is proposed and presented in Scheme 1. For the radical pathway, it has been proved that $SO_4^{\cdot-}$, $^{\cdot}OH$ and $O_2^{\cdot-}$ participate in the reaction. Since $S_2O_8^{2-}$ itself is incapable of generating $^{\cdot}OH$, it must be derived from H_2O or OH^- (Howard Jr and Levitt, 1953). This process should be assisted by external energy, such as UV, thermal, ultrasound and catalyst. Previous studies demonstrated the sp^2 carbons, defective edges and ketone groups were chemically active to stimulate persulfate decomposition and generate radicals (Duan et al., 2016a; Duan et al., 2016b). The electron-rich regions (e.g. the sp^2-carbon with defective edge and ketonic groups) on FBBC-800 could affect the electronic configuration of PDS (especially the O-O

bond in $S_2O_8^{2-}$) to form the "semi-active" $S_2O_8^{2-}$ complex. In this case, the hydrolysis reaction of PDS was activated (Eq. (7)). Then the produced HO_2^- would react with another $S_2O_8^{2-}$ quickly and the $SO_4^{\cdot-}$ and $O_2^{\cdot-}$ was generated (Eq. (8)). Meanwhile, $SO_4^{\cdot-}$ could quickly transform into $^{\cdot}OH$ through Eq. (9) ($k= 7\times10^7\ M^{-1}\ s^{-1}$) (Liu et al., 2016), which might be the reason for the strong $^{\cdot}OH$ signals and weak $SO_4^{\cdot-}$ signals in ESR. As to $^1O_2$, an important species in the non-radical pathway, the detailed generation mechanism has not been fully understood. A possible pathway could be through the reaction of $O_2^{\cdot-}$ and H_2O based on Eq. (10) and the C=O group played an important role (Cheng et al., 2017).

$$S_2O_8^{2-} + 2H_2O \rightarrow HO_2^- + 2SO_4^{2-} + 3H^+ \quad \text{Eq. (7)}$$

$$S_2O_8^{2-} + HO_2^- \rightarrow SO_4^{2-} + SO_4^{\cdot-} + O_2^{\cdot-} + H^+ \quad \text{Eq. (8)}$$

$$SO_4^{\cdot-} + OH^- \rightarrow SO_4^{2-} + {}^{\cdot}OH \quad \text{Eq. (9)}$$

$$2O_2^{\cdot-} + 2H_2O \rightarrow H_2O_2 + 2OH^- + {}^1O_2 \quad \text{Eq. (10)}$$

$$\text{FBBC} + \text{PDS} \rightarrow [\text{FBBC-PDS}^*] \text{ complex} \quad \text{Eq. (11)}$$

$$S_2O_8^{2-} + 2e^- \rightarrow 2SO_4^{2-} \quad \text{Eq. (12)}$$

As mentioned above, the formation of charge transfer intermediates between PDS and FBBC-800 accelerate the decomposition of PDS and initiate the subsequent radical generation reaction for phenol degradation. Besides, the direct electron transfer in the non-radical pathway also contributes to the degradation of phenol. When both PDS and phenol adhere to the FBBC-800, the ternary system is formed, where the electron can be abstracted from adsorbed phenol (electron donor) to metastable FBBC-PDS* complexes (electron receptor), with FBBC-800 as

electron medium (Eq. (11)) (Ren et al. 2019). The O-O bond in PDS is cleaved by accepting the electron and finally decomposed into SO_4^{2-} (Eq. (12)). To prove the point, K_2CrO_4 as an electron trapping agent was added in the PDS system. The inhibited effect as shown in Fig. 3d proved the occurrence of electron transfer. For further analysis, some electrochemical measurements were conducted. The impedance of carbon-based catalyst is an important parameter affecting the electron transfer, which can be obtained from the Nyquist plots in EIS. The largely decreased semicircle diameter of FBBC-800 indicated its better conductivity than the blank solution with bare GCE (Fig. 7a). Besides, FBBC-800 exhibited a much smaller semicircle than SSBC-400, manifesting the better conductivity of FBBC-800 (Fig. S6). This may be an important factor for the much higher catalytic efficiency of FBBC-800 than FBBC-400. In addition, as can be seen from the chronoamperometry test (Fig. 7b), the current change was observed after injection of PDS and phenol, which provided direct evidence of electron transfer among FBBC-800, PDS and phenol molecules. The LSV curves (Fig. 7c) also demonstrated the increased current after addition of PDS, suggesting the formation of metastable complexes between PDS and FBBC-800. Besides, the current was further increased after addition of phenol, which might be ascribed to the electron transfer between phenol, FBBC-800 and PDS. Totally, in the synergistic effect of radical and non-radical pathway, the phenol was completely oxidized. The possible degradation pathway of phenol was provided in Fig. S7.

3.6. Practical application

The interference of several background substances on the catalytic efficiency of FBBC-800/PDS system was investigated (Yi et al., 2019). As shown in Fig. S8a, the impact of Cl^- and HA was insignificant, but HCO_3^- and HPO_4^{2-} slightly inhibited phenol degradation. The degradation efficiency decreased from 100% to 74% for HCO_3^- and to 80% for HPO_4^{2-}. This phenomenon may be ascribed to scavenging effect of HCO_3^- and HPO_4^{2-}. To investigate the practical efficiency of FBBC-800 in real water matrix, samples taken from Xiangjiang River and Taozi Lake were used for experiment. Efficient removal of phenol was still obtained in river water and lake water within 60 minutes, which confirmed the applicability of FBBC-800/PDS system for realistic water environment remediation (Fig. S8b). Besides, the degradation efficiency of FBBC-800/PDS to pharmaceutical wastewater was also studied. As the component of pharmaceutical wastewater was complicated with high concentration of various organic compounds, three-dimensional excitation Emission matrix fluorescence spectra was used to characterize the degree of organic pollution. Fig. S8c-d showed that the fluorescence intensity of pharmaceutical wastewater samples had significantly decreased after reaction, indicating the effectiveness of FBBC-800/PDS system in complex water environment. In addition to phenol, the degradation of other three typical pollutants was also conducted, including rhodamine B, tetracycline hydrochloride and 2,4-dichlorophenol. Result in Fig. S8e demonstrated the universality of FBBC-800/PDS system for organic pollutants degradation.

4. Conclusion

This study developed a low cost and high efficient catalyst by simple pyrolysis of fishbone and used it for persulfate activation. Pyrolysis temperature largely affects the catalytic efficiency of FBBC, with the order of FBBC-800 (100%) > FBBC-600 (65.1%) > FBBC-400 (4.7%). A complete removal of phenol is achieved within 60 min at the FBBC-800 dosage of 0.1 g/L and in a wide pH range (3.0-9.0). Compared with other recently reported metal free catalysts, the FBBC-800 shows competitive or even better catalytic efficiency, simpler preparation process and lower cost. The high surface area, electron transfer capacity, abundant oxygen group and defective structure endow the FBBC-800 with good catalytic activity. Based on the radical quenching experiment, ESR test and electrochemical characterization, both radical and non-radical pathways take part in the reaction, and electron transfer plays an important role in this process. Moreover, he FBBC-800/PDS system exhibits good performance in real water environment, demonstrating its practical application potential. This study provides a new insight into biowaste reutilization and the structure regulation of carbon-based catalyst. Further research may keep on exploitation of the biowaste with hierarchical structure and chemical components for the preparation of highly efficient and reusable catalyst.

Acknowledgments

The study was financially supported by the Program for Changjiang Scholars and Innovative Research Team in University (IRT-13R17), the National Natural Science Foundation of China (51521006, 51579096), the Three Gorges Follow-up Research

Project (2017HXXY-05), and the Funds for Innovative Province Construction of Hunan Province of China (2019RS3012).

References:

Akagündüz, Y., Mosquera, M., Giménez, B., Alemán, A., Montero, P., Gómez-Guillén, M.C., 2014. Sea bream bones and scales as a source of gelatin and ACE inhibitory peptides. LWT-Food. Sci. Technol. 55, 579-585. DOI: https://doi.org/10.1016/j.lwt.2013.10.026.

Alhokbany, N., Ahama, T., Ruksana, Naushad, M., Alshehri, S.M., 2019. AgNPs embedded N- doped highly porous carbon derived from chitosan based hydrogel as catalysts for the reduction of 4-nitrophenol. Composites Part B: Engineering, 173, 106950. DOI: https://doi.org/10.1016/j.compositesb.2019.106950.

Alshehri, S.M., Naushad, M., Ahamad, T., Alothman, Z.A., Aldalbahi, A., 2014. Synthesis, characterization of curcumin based ecofriendly antimicrobial bio-adsorbent for the removal of phenol from aqueous medium. Chem. Eng. J., 254, 181-189. DOI: https://doi.org/10.1016/j.cej.2014.05.100.

Bao, Y., Lim, T.T., Wang, R., Webster, R.D., Hu, X., 2018. Urea-assisted one-step synthesis of cobalt ferrite impregnated ceramic membrane for sulfamethoxazole degradation via peroxymonosulfate activation. Chem. Eng. J. 343, 737-747. DOI: https://doi.org/10.1016/j.cej.2018.03.010.

Bommier, C., Xu, R., Wang, W., Wang, X., Wen, D., Lu, J., Ji, X., 2015. Self-activation of cellulose: A new preparation methodology for activated carbon electrodes in electrochemical capacitors. Nano Energy, 13, 709-717. DOI: https://doi.org/10.1016/j.nanoen.2015.03.022.

521 Boutinguiza, M., Pou, J., Comesaña, R., Lusquiños, F., de Carlos, A., León, B.,
522 2012. Biological hydroxyapatite obtained from fish bones. Mat. Sci. Eng.
523 C-Mater. 32, 478-486. DOI: https://doi.org/10.1016/j.msec.2011.11.021.
524 Buxton, G.V., Greenstock, C.L., Helman, W.P., Ross, A.B., 1988. Critical review of
525 rate constants for reactions of hydrated electrons, hydrogen atoms and
526 hydroxyl radicals ($\cdot OH/\cdot O^-$ in aqueous solution. J. Phys. Chem. Ref. Data 17,
527 513-886. DOI: https://doi.org/10.1063/1.555805.
528 Chakraborty, R., RoyChowdhury, D., 2013. Fish bone derived natural
529 hydroxyapatite-supported copper acid catalyst: Taguchi optimization of
530 semibatch oleic acid esterification. Chem. Eng. J., 215-216, 491-499. DOI:
531 https://doi.org/10.1016/j.cej.2012.11.064.
532 Chen, C., Ma, T., Shang, Y., Gao, B., Jin, B., Dan, H., Li, Q., Yue, Q., Li, Y., Wang,
533 Y., Xu, X., 2019. In-situ pyrolysis of Enteromorpha as carbocatalyst for
534 catalytic removal of organic contaminants: Considering the intrinsic N/Fe in
535 Enteromorpha and non-radical reaction. Appl. Catal. B-Environ. 250, 382-395.
536 DOI: https://doi.org/10.1016/j.apcatb.2019.03.048.
537 Cheng, X., Guo, H., Zhang, Y., Wu, X., Liu, Y., 2017. Non-photochemical
538 production of singlet oxygen via activation of persulfate by carbon nanotubes.
539 Water Res. 113, 80-88. DOI: https://doi.org/10.1016/j.watres.2017.02.016 .
540 Dhiman, P., Naushad, M., Batoo, K.M., Kumar, A., Sharma, G., Ghfar, A.A.,
541 Kumar, G., Singh, M., 2017. Nano $Fe_xZn_{1-x}O$ as a tuneable and efficient
542 photocatalyst for solar powered degradation of bisphenol A from aqueous

environment. J. Clean. Prod., 165, 1542-1556. DOI: https://doi.org/10.1016/j.jclepro.2017.07.245.

Duan, X., Su, C., Zhou, L., Sun, H., Suvorova, A., Odedairo, T., Zhu, Z., Shao, Z., Wang, S., 2016. Surface controlled generation of reactive radicals from persulfate by carbocatalysis on nanodiamonds. Appl. Catal. B: Environ. 194, 7-15. DOI: https://doi.org/10.1016/j.apcatb.2016.04.043 .

Duan, X., Sun, H., Ao, Z., Zhou, L., Wang, G., Wang, S., 2016. Unveiling the active sites of graphene-catalyzed peroxymonosulfate activation. Carbon 107, 371-378. DOI: https://doi.org/10.1016/j.carbon.2016.06.016.

Duan, X., Sun, H., Kang, J., Wang, Y., Indrawirawan, S., Wang, S., 2015. Insights into Heterogeneous Catalysis of Persulfate Activation on Dimensional-Structured Nanocarbons. ACS Catal. 5, 4629-4636. DOI: https://doi.org/10.1021/acscatal.5b00774.

Fang, G., Liu, C., Gao, J., Dionysiou, D.D., Zhou, D., 2015. Manipulation of Persistent Free Radicals in Biochar To Activate Persulfate for Contaminant Degradation. Environ. Sci. Technol. 49, 5645-5653. DOI: https://doi.org/10.1021/es5061512.

FAO: The State of World Fisheries and Aquaculture, 2020. Food and agriculture organization of the United Nations. Avaliable from http://www.fao.org.

Ho, S., Chen, Y., Li, R., Zhang, C., Ge, Y., Cao, G., Ma, M., Duan, X., Wang, S., Ren, N., 2019. N-doped graphitic biochars from C-phycocyanin extracted Spirulina residue for catalytic persulfate activation toward nonradical

disinfection and organic oxidation. Water Res. 159, 77-86. DOI: https://doi.org/10.1016/j.watres.2019.05.008.

Howard Jr, E., Levitt, L.S., 1953. The Persulfate Oxidation of Sulfoxides in Buffered Solution. 1 I. J. Am. Chem. Soc. 75, 6170-6173. DOI: https://doi.org/10.1021/ja01120a018.

Kambo, H.S., Dutta, A., 2015. A comparative review of biochar and hydrochar in terms of production, physico-chemical properties and applications. Renewable and Sustainable Energy Reviews, 45, 359-378. DOI: https://doi.org/10.1016/j.rser.2015.01.050.

Kim, S., Lee, Y., Andrew Lin, K., Hong, E., Kwon, E.E., Lee, J., 2020. The valorization of food waste via pyrolysis. J. Clean. Prod. 259, 120816. DOI: https://doi.org/10.1016/j.jclepro.2020.120816.

Kumar, A., Kumar, A., Sharma, G., Al-Muhtaseb, A.H., Naushad, M., Ghfar, A.A., Guo, C., Stadler, F.J., 2018. Biochar-templated g-C_3N_4/$Bi_2O_2CO_3$/$CoFe_2O_4$ nano-assembly for visible and solar assisted photo-degradation of paraquat, nitrophenol reduction and CO_2 conversion. Chem. Eng. J., 339, 393-410. DOI: https://doi.org/10.1016/j.cej.2018.01.105.

Liu, H., Bruton, T.A., Li, W., Buren, J.V., Prasse, C., Doyle, F.M., Sedlak, D.L., 2016. Oxidation of Benzene by Persulfate in the Presence of Fe(III)- and Mn(IV)-Containing Oxides: Stoichiometric Efficiency and Transformation Products. Environ. Sci. Technol. 50, 890-8. DOI: https://doi.org/10.1021/acs.est.5b04815.

587 Ma, W., Wang, N., Du, Y., Xu, P., Sun, B., Zhang, L., Lin, K.A., 2018.
588 Human-Hair-Derived N, S-Doped Porous Carbon: An Enrichment and
589 Degradation System for Wastewater Remediation in the Presence of
590 Peroxymonosulfate. ACS Sustain. Chem. Eng. 7, 2718-2727. DOI:
591 https://doi.org/10.1021/acssuschemeng.8b05801.
592 Marti-Quijal, F.J., Remize, F., Meca, G., Ferrer, E., Ruiz, M.A., Barba, F.J., 2020.
593 Fermentation in fish and by-products processing: an overview of current
594 research and future prospects. Curr. Opin. Food Sci. 9-16. DOI:
595 https://doi.org/10.1016/j.cofs.2019.08.001.
596 Medellín-Castillo, N.A., Cruz-Briano, S.A., Leyva-Ramos, R., Moreno-Piraján, J.C.,
597 Torres-Dosal, A., Giraldo-Gutiérrez, L., Labrada-Delgado, G.J., Pérez, R.O.,
598 Rodriguez-Estupiñan, J.P., Reyes Lopez, S.Y., Berber Mendoza, M.S., 2020.
599 Use of bone char prepared from an invasive species, pleco fish
600 (Pterygoplichthys spp.), to remove fluoride and Cadmium(II) in water. J.
601 Environ. Manage. 256, 109956. DOI:
602 https://doi.org/10.1016/j.jenvman.2019.109956.
603 Medellin-Castillo, N.A., Leyva-Ramos, R., Padilla-Ortega, E., Perez, R.O.,
604 Flores-Cano, J.V., Berber-Mendoza, M.S., 2014. Adsorption capacity of bone
605 char for removing fluoride from water solution. Role of hydroxyapatite content,
606 adsorption mechanism and competing anions. J. Ind. Eng. Chem. 20,
607 4014-4021. DOI: https://doi.org/10.1016/j.jiec.2013.12.105.
608 Naushad, M., Alqadami, A.A., AlOthman, Z.A., Alsohaimi, I.H., Algamdi, M.S.,

609 Aldawsari, A.M., 2019a. Adsorption kinetics, isotherm and reusability studies
610 for the removal of cationic dye from aqueous medium using arginine modified
611 activated carbon. J. Mol. Liq., 293, 111442. DOI:
612 https://doi.org/10.1016/j.molliq.2019.111442.
613 Naushad, M., Sharma, G., Alothman, Z.A., 2019b. Photodegradation of toxic dye
614 using Gum Arabic-crosslinked-poly(acrylamide)/Ni(OH)$_2$/FeOOH
615 nanocomposites hydrogel. J. Clean. Prod., 241, 118263. DOI:
616 https://doi.org/10.1016/j.jclepro.2019.118263.
617 Nawaz, A., Li, E., Irshad, S., Xiong, Z., Xiong, H., Shahbaz, H.M., Siddique, F.,
618 2020. Valorization of fisheries by-products: Challenges and technical concerns
619 to food industry. Trends Food Sci. Tech. 99, 34-43. DOI:
620 https://doi.org/10.1016/j.tifs.2020.02.028.
621 Neta, P., Huie, R.E., Ross, A.B., 1988. Rate Constants for Reactions of Inorganic
622 Radicals in Aqueous Solution. J. Phys. Chem. Ref. Data. 17(3), 1027-1284.
623 DOI: https://doi.org/10.1063/1.555808.
624 Niu, L., Shen, C., Yan, L., Zhang, J., Lin, Y., Gong, Y., Li, C., Sun, C.Q., Xu, S.,
625 2019. Waste bones derived nitrogen‐doped carbon with high micropore ratio
626 towards supercapacitor applications. J. Colloid Interf. Sci. 547, 92-101. DOI:
627 https://doi.org/10.1016/j.jcis.2019.03.097.
628 Niu, J., Shao, R., Liu, M., Zan, Y., Dou, M., Liu, J., Zhang, Z., Huang, Y., Wang, F.,
629 2019. Porous Carbons Derived from Collagen‐Enriched Biomass: Tailored
630 Design, Synthesis, and Application in Electrochemical Energy Storage and

631 Conversion. Adv. Funct. Mater., 29, 1905095. DOI:
632 https://doi.org/10.1002/adfm.201905095.
633 Oh, W., Lisak, G., Webster, R.D., Liang, Y., Veksha, A., Giannis, A., Moo, J.G.S.,
634 Lim, J., Lim, T., 2018. Insights into the thermolytic transformation of
635 lignocellulosic biomass waste to redox-active carbocatalyst: Durability of
636 surface active sites. Appl. Catal. B: Environ. 233, 120-129. DOI:
637 https://doi.org/10.1016/j.apcatb.2018.03.106.
638 Qin, L., Yi, H., Zeng, G., Lai, C., Huang, D., Xu, P., Fu, Y., He, J., Li, B., Zhang,
639 C., 2019. Hierarchical porous carbon material restricted Au catalyst for highly
640 catalytic reduction of nitroaromatics. J. Hazard. Mater. 380, 120864. DOI:
641 https://doi.org/10.1016/j.jhazmat.2019.120864.
642 Rao, P.S., Hayon, E., 1975. Redox potentials of free radicals. IV. Superoxide and
643 hydroperoxy radicals. O_2^- and HO_2. J. Phys. Chem. 79, 397-402. DOI:
644 https://doi.org/10.1021/j100571a021.
645 Ren, W., Xiong, Z., Nie, G., Zhang, H., Duan, X., Wang, S., 2019. Insights into the
646 Electron-Transfer Regime of Peroxydisulfate Activation on Carbon Nanotubes:
647 The Role of Oxygen Functional Groups. Environ. Sci. Technol., 54, 1267-1275.
648 DOI: https://doi.org/10.1021/acs.est.9b06208.
649 Senthil Kumar, P., Ramakrishnan, K., Dinesh Kirupha, S., Sivanesan, S., 2011.
650 Thermodynamic, kinetic, and equilibrium studies on phenol removal by use of
651 cashew nut shell. The Canadian Journal of Chemical Engineering, 89, 284-291.
652 DOI: 10.1002/cjce.20396.

653 Song, B., Zeng, Z., Zeng, G., Gong, J., Xiao, R., Ye, S., Chen, M., Lai, C., Xu, P.,
654 Tang, X., 2019. Powerful combination of g-C_3N_4 and LDHs for enhanced
655 photocatalytic performance: A review of strategy, synthesis, and applications.
656 Adv. Colloid Interfac. 272, 101999. DOI:
657 https://doi.org/10.1016/j.cis.2019.101999.
658 Sun, C., Chen, T., Huang, Q., Zhan, M., Li, X., Yan, J., 2020. Activation of
659 persulfate by CO_2-activated biochar for improved phenolic pollutant
660 degradation: Performance and mechanism. Chem. Eng. J. 380, 122519. DOI:
661 https://doi.org/10.1016/j.cej.2019.122519.
662 Tang, L., Liu, Y., Wang, J., Zeng, G., Deng, Y., Dong, H., Feng, H., Wang, J., Peng,
663 B., 2018. Enhanced activation process of persulfate by mesoporous carbon for
664 degradation of aqueous organic pollutants: Electron transfer mechanism. Appl.
665 Catal. B: Environ. 231, 1-10. DOI:
666 https://doi.org/10.1016/j.apcatb.2018.02.059.
667 Toppe, J., Albrektsen, S., Hope, B., Aksnes, A., 2007. Chemical composition,
668 mineral content and amino acid and lipid profiles in bones from various fish
669 species. Comp. Biochem. Physiol. B, Biochem. Mol. Biol. 146, 395-401. DOI:
670 10.1016/j.cbpb.2006.11.020.
671 Wacławek, S., Lutze, H.V., Grübel, K., Padil, V.V.T., Černík, M., Dionysiou, D.D.,
672 2017. Chemistry of persulfates in water and wastewater treatment: A review.
673 Chem. Eng. J. 330, 44-62. DOI: https://doi.org/10.1016/j.cej.2017.07.132.
674 Wang, H., Guo, W., Liu, B., Wu, Q., Luo, H., Zhao, Q., Si, Q., Sseguya, F., Ren, N.,

675 2019a. Edge-nitrogenated biochar for efficient peroxydisulfate activation: An
676 electron transfer mechanism. Water Res. 160, 405-414. DOI:
677 https://doi.org/10.1016/j.watres.2019.05.059.
678 Wang, H., Wang, K., Song, H., Li, H., Ji, S., Wang, Z., Li, S., Wang, R., 2015.
679 N-doped porous carbon material made from fish-bones and its highly
680 electrocatalytic performance in the oxygen reduction reaction. RSC Adv. 5,
681 48965-4897. DOI: https://doi.org/10.1039/C5RA09144F.
682 Wang, H., Zeng, Z., Xu, P., Li, L., Zeng, G., Xiao, R., Tang, Z., Huang, D., Tang,
683 L., Lai, C., 2019b. Recent progress in covalent organic framework thin films:
684 fabrications, applications and perspectives. Chem. Soc. Rev. 48, 488-516. DOI:
685 https://doi.org/10.1039/C8CS00376A.
686 Wang, J., Wang, S., 2018. Activation of persulfate (PS) and peroxymonosulfate
687 (PMS) and application for the degradation of emerging contaminants. Chem.
688 Eng. J. 334, 1502-1517. DOI: https://doi.org/10.1016/j.cej.2017.11.059.
689 Yang, Y., Zhang, C., Huang, D., Zeng, G., Huang, J., Lai, C., Zhou, C., Wang, W.,
690 Guo, H., Xue, W., 2018. Boron nitride quantum dots decorated ultrathin porous
691 g-C3N4: Intensified exciton dissociation and charge transfer for promoting
692 visible-light-driven molecular oxygen activation. Appl. Catal. B: Environ. DOI:
693 https://doi.org/10.1016/j.apcatb.2018.12.049.
694 Ye, S., Yan, M., Tan, X., Liang, J., Zeng, G., Wu, H., Song, B., Zhou, C., Yang, Y.,
695 Wang, H., 2019. Facile assembled biochar-based nanocomposite with
696 improved graphitization for efficient photocatalytic activity driven by visible

light. Appl. Catal. B: Environ. 250, 78-88. DOI: https://doi.org/10.1016/j.apcatb.2019.03.004.

Yi, H., Yan, M., Huang, D., Zeng, G., Lai, C., Li, M., Huo, X., Qin, L., Liu, S., Liu, X., Li, B., Wang, H., Shen, M., Fu, Y., Guo, X., 2019. Synergistic effect of artificial enzyme and 2D nano-structured Bi_2WO_6 for eco-friendly and efficient biomimetic photocatalysis. Appl. Catal. B: Environ. 250, 52-62. DOI: https://doi.org/10.1016/j.apcatb.2019.03.008.

Yin, T., Park, J.W., Xiong, S., 2015. Physicochemical properties of nano fish bone prepared by wet media milling. LWT-Food. Sci. Technol. 64, 367-373. DOI: https://doi.org/10.1016/j.lwt.2015.06.007.

Yu, J., Tang, L., Pang, Y., Zeng, G., Wang, J., Deng, Y., Liu, Y., Feng, H., Chen, S., Ren, X., 2019. Magnetic nitrogen-doped sludge-derived biochar catalysts for persulfate activation: Internal electron transfer mechanism. Chem. Eng. J. 364, 146-159. DOI: https://doi.org/10.1016/j.cej.2019.01.163.

Zhang, J., Wang, Q., 2016. Sustainable mechanisms of biochar derived from brewers' spent grain and sewage sludge for ammonia–nitrogen capture. J. Clean. Prod., 112, 3927-3934. DOI: https://doi.org/10.1016/j.jclepro.2015.07.096.

Zhang, J., Yin, T., Xiong, S., Li, Y., Ikram, U., Liu, R., 2016. Thermal treatments affect breakage kinetics and calcium release of fish bone particles during high-energy wet ball milling. J. Food Eng. 183, 74-80. DOI: https://doi.org/10.1016/j.jfoodeng.2016.03.027.

719 Zhao, Y., Feng, D., Zhang, Y., Huang, Y., Sun, S., 2016. Effect of pyrolysis
720 temperature on char structure and chemical speciation of alkali and alkaline
721 earth metallic species in biochar. Fuel Process. Technol., 141, 54-60. DOI:
722 https://doi.org/10.1016/j.fuproc.2015.06.029.
723 Zhu, S., Huang, X., Ma, F., Wang, L., Duan, X., Wang, S., 2018. Catalytic Removal
724 of Aqueous Contaminants on N-Doped Graphitic Biochars: Inherent Roles of
725 Adsorption and Nonradical Mechanisms. Environ. Sci. Technol. 52, 8649-8658.
726 DOI: https://doi.org/10.1021/acs.est.8b01817.
727
728

CAPTIONS

Fig. 1. (a) SEM of FBBC-800; (b, c) TEM of FBBC-800; TEM element mapping of FBBC-800: (d) carbon , (e) nitrogen and (f) oxygen.

Fig. 2. (a) Adsorption removal and (b) Oxidation degradation of phenol; (c) Effects of PDS dosage; (d) FBBC-800 dosage; (e) Initial pH of solution; (f) Phenol concentration. Conditions: [biochar] = 0.1 g/L, [PDS] = 1.0 g/L, [temperature] = 25 ℃, [phenol] = 20 mg/L.

Fig. 3. Effects of (a) MeOH, (b)TBA and (c) EtOH on phenol degradation at different molar ratio with PDS; (d) Effects of NaN_3, BQ and K_2CrO_4 on phenol degradation. Conditions: [FBBC-800] = 0.1 g/L, [PDS] = 1.0 g/L, [temperature] = 25 ℃, [phenol] = 20 mg/L.

Fig. 4. ESR spectra of PDS activation by FBBC-800.

Fig. 5. (a) Nitrogen adsorption and desorption curves, (b) pore size distribution, (c) XPS survey and (d) Raman spectra of FBBC-800 before and after reaction.

Fig. 6. O1s high resolution scans of (a) FBBC-800 before reaction and (b) FBBC-800 after reaction; N1s high resolution scans of (c) FBBC-800 before reaction and (d) FBBC-800 after reaction.

Fig. 7. (a) Electrochemical impedance spectroscopy (EIS) of bare GCE and FBBC-800 loaded on GCE; (b) the current–time (I-t) curves of FBBC-800 and (c) Linear sweep voltammetry (LSV) curves under different conditions.

Scheme 1. Proposed mechanism of FBBC-800 to activate PDS for phenol degradation

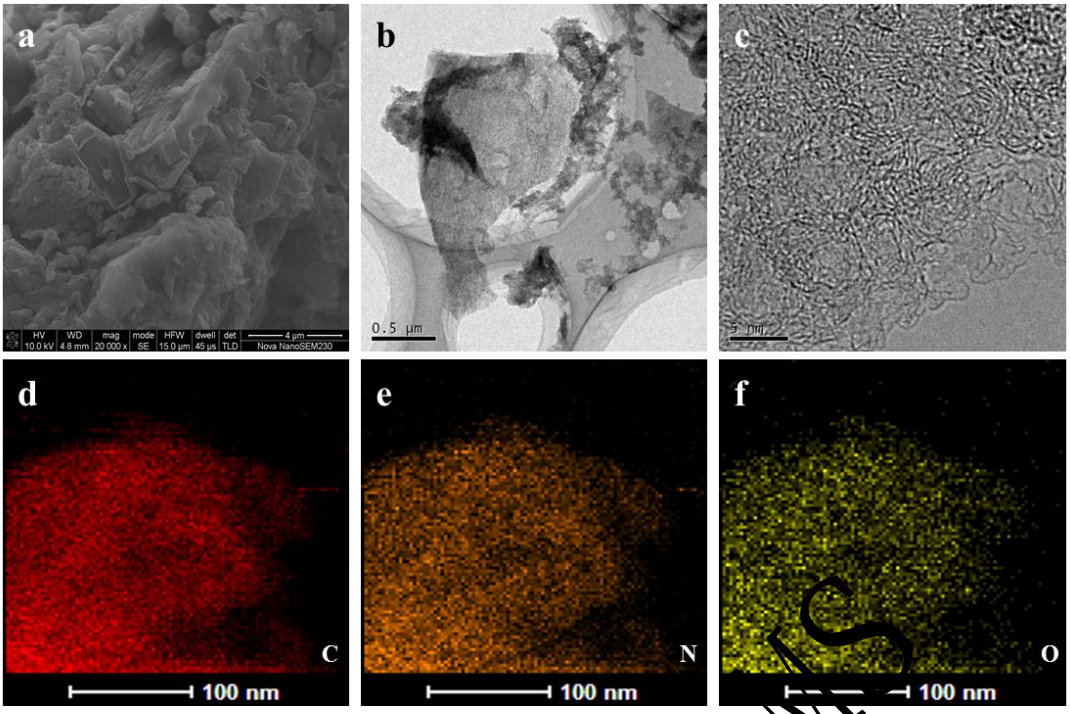

Fig. 1. (a) SEM of FBBC-800; (b, c) TEM of FBBC-800; TEM element mapping of FBBC-800: (d) carbon , (e) nitrogen and (f) oxygen.

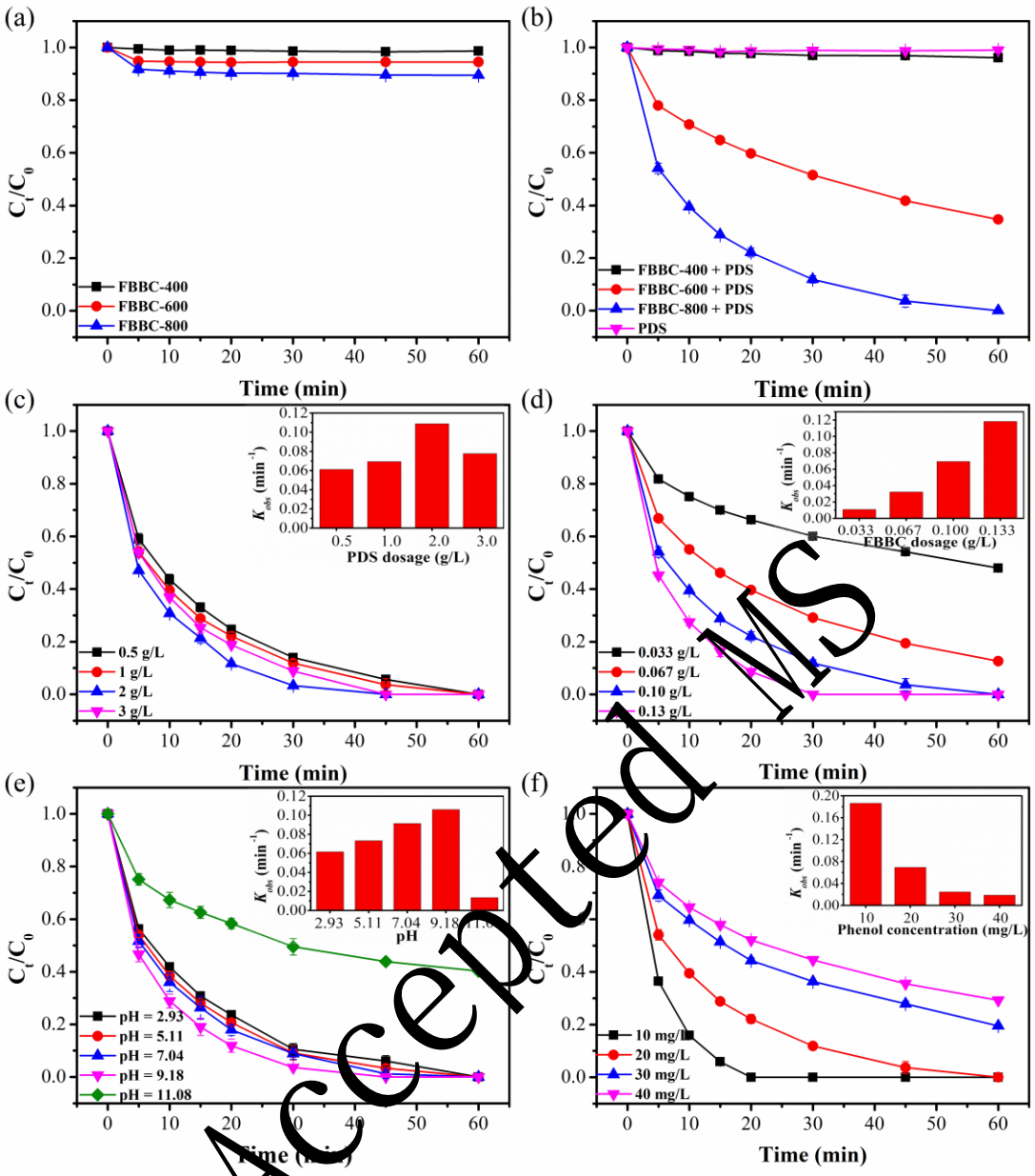

Fig. 2. (a) Adsorption removal and (b) Oxidation degradation of phenol; (c) Effects of PDS dosage; (d) FBBC-800 dosage; (e) Initial pH of solution; (f) Phenol concentration. Conditions: [biochar]=0.1 g/L, [PDS]=1.0 g/L, [temperature]=25 ℃, [phenol]=20 mg/L. Insets are the corresponding changes of pseudo-first-order rate constant.

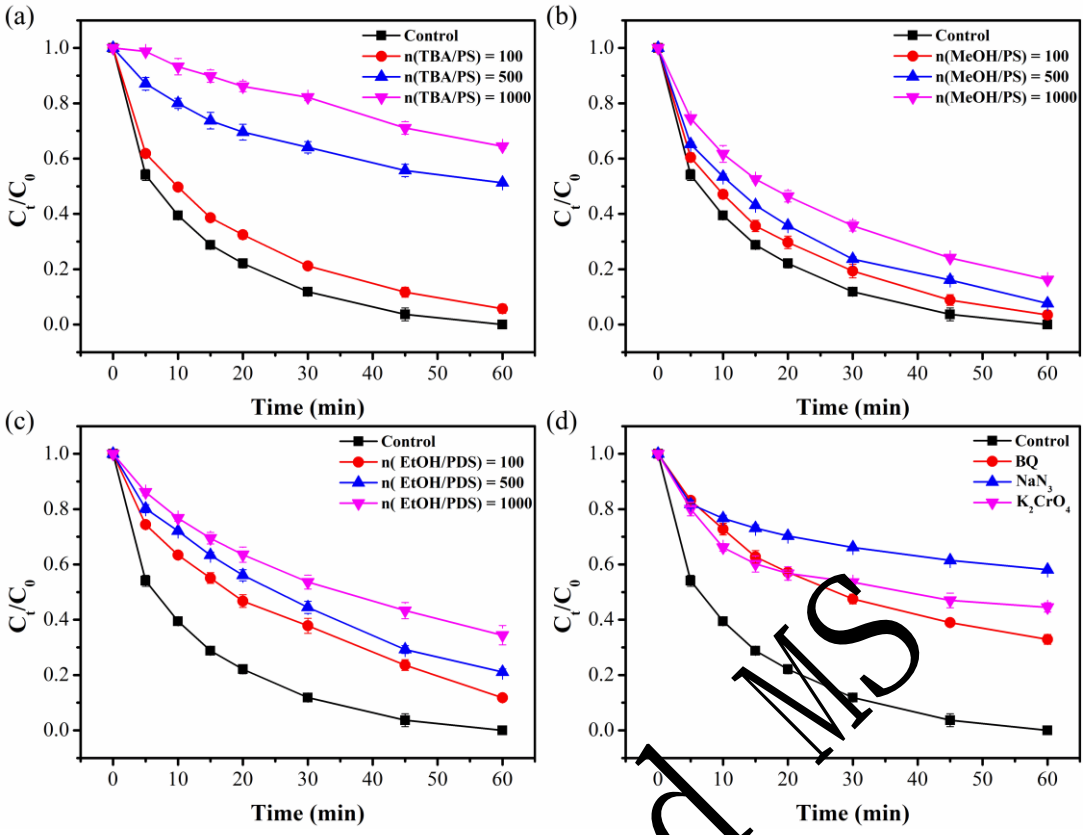

Fig. 3. Effects of (a) MeOH, (b)TBA, and (c) EtOH on phenol degradation at different molar ratio with PDS; (d) Effects of NaN_3, BQ and K_2CrO_4 on phenol degradation. Conditions: [FBBC-800]=0.1 g/L, [PDS]=1.0 g/L,[temperature]=25 ℃, [phenol]=20 mg/L.

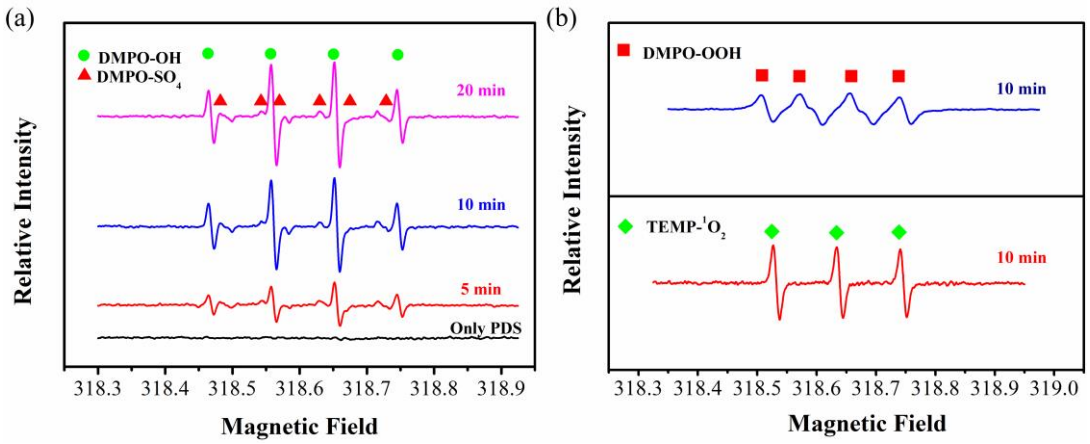

772
773
774 **Fig. 4.** ESR spectra of PDS activation by FBBC-800.
775
776

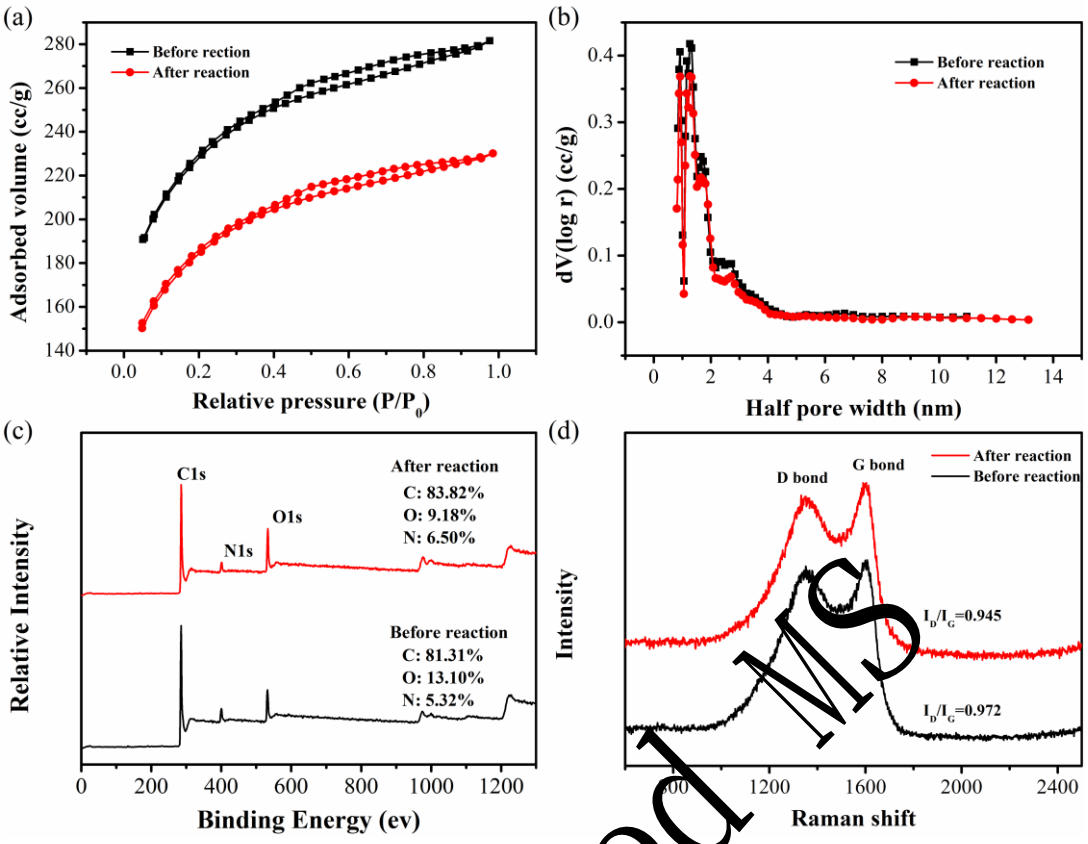

Fig. 5. (a) Nitrogen adsorption and desorption curves, (b) pore size distribution, (c) XPS survey and (d) Raman spectra of FBBC-800 before and after reaction.

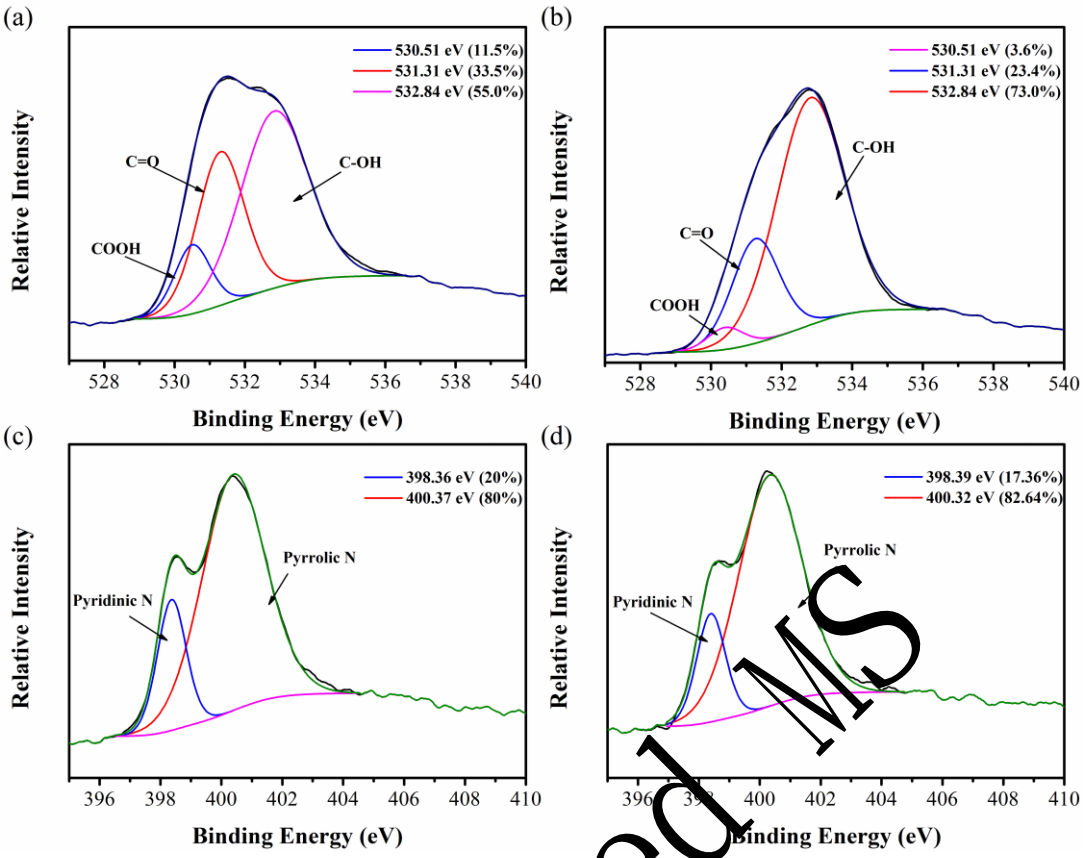

Fig. 6. O1s high resolution scans of (a) FBBC-800 before reaction and (b) FBBC-800 after reaction; N1s high resolution scans of (c) FBBC-800 before reaction and (d) FBBC-800 after reaction.

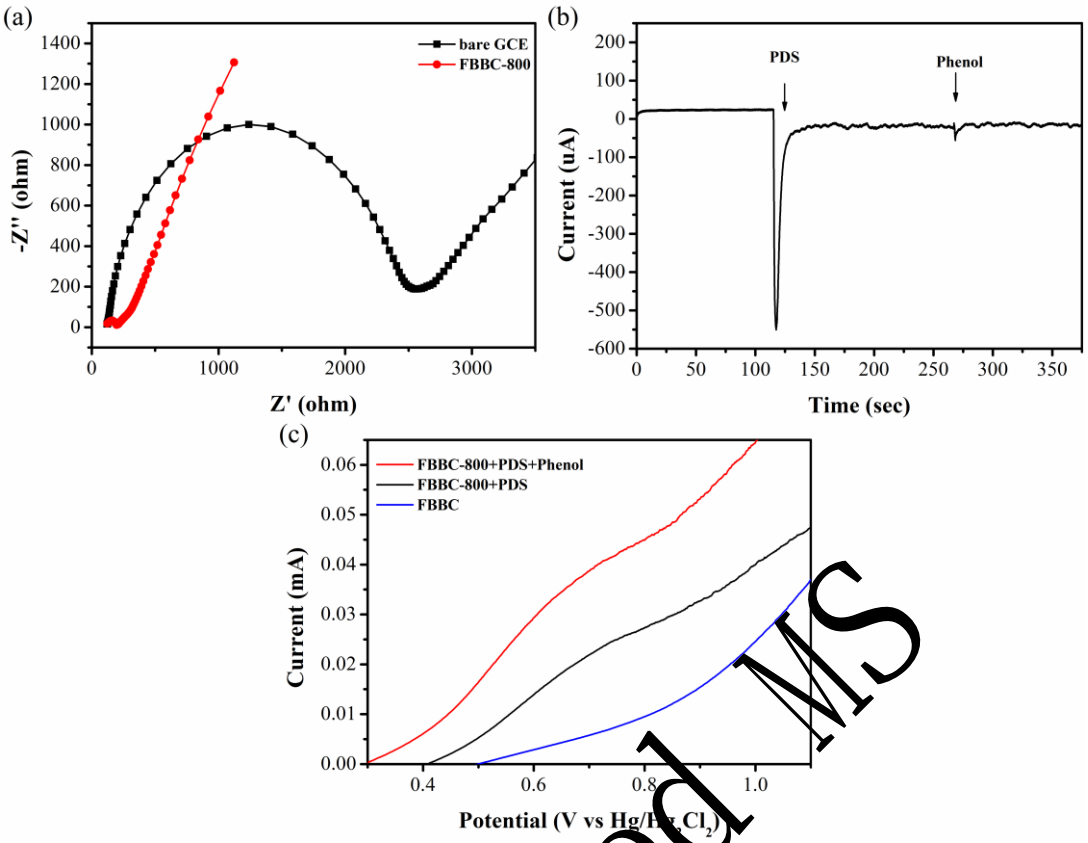

791

792

793 **Fig. 7.** (a) Electrochemical impedance spectroscopy (EIS) of bare GCE and
794 FBBC-800 loaded on GCE; (b) the current–time (I-t) curves of FBBC-800 and (c)
795 Linear sweep voltammetry (LSV) curves under different conditions.

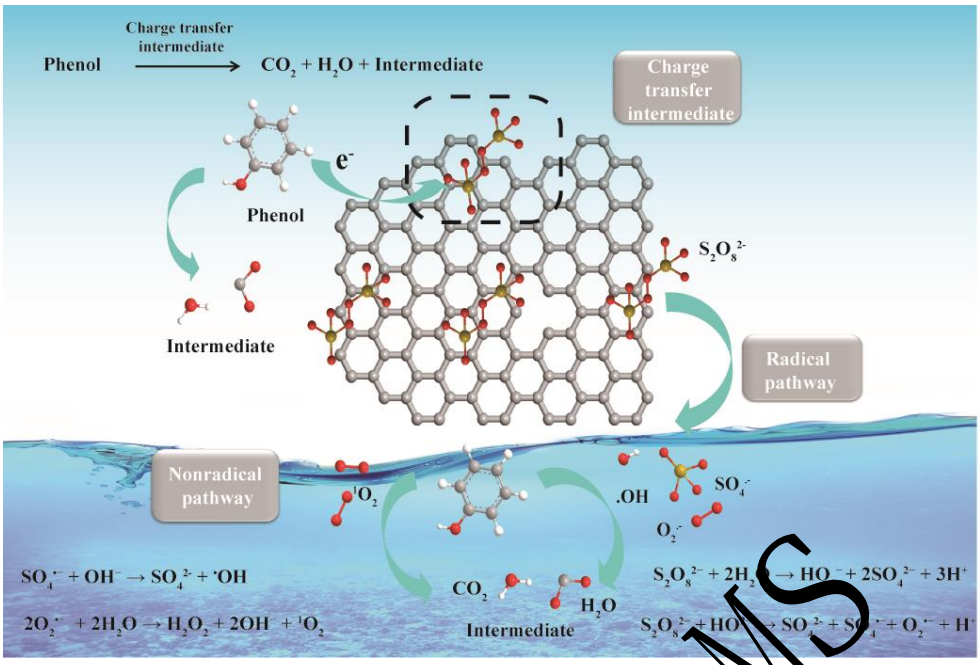

Scheme 1. Proposed mechanism of FBBC-800 to activate PDS for phenol degradation

802 Abbreviation List

803

Abbreviation	Full name
FBBC	Fishbone derived biochar
k_{obs}	Reaction rate constant
PS-AOPs	Persulfate-induced advanced oxidation processes
PDS	Peroxydisulfate
·OH	Hydroxyl radicals
$SO_4^{\cdot -}$	Sulfate radicals
$O_2^{\cdot -}$	Superoxide radical
$^1O_2$	Singlet oxygen
ESR	Electron spin resonance spectrometer
FTIR	Fourier-transform infrared spectroscopy
SEM	Scanning electronic microscopy
HRTEM	High-resolution transmission electron microscopy
FTIR	Fourier-transform infrared spectroscopy
XPS	X-ray photoelectron spectroscopy
EIS	Electrochemical impedance spectroscopy
LSV	Liner sweep voltammetry
MeOH	Methanol
TBA	Tert-butyl-alcohol
EtOH	Ethanol
BQ	p-benzoquinone
DMPO	5,5-dimethyl-1-pyrroline N-oxide
TMP	2,2,6,6-tetramethyl-4-piperidinol

804